



The influence of residual tin following induction melt thermoforming of composite parts

Iain Campbell^{*}, Daniel M. Mulvihill, Philip Harrison

Materials and Manufacturing Research Group, James Watt School of Engineering, University of Glasgow, University Avenue, Glasgow G12 8QQ, UK

ARTICLE INFO

Keywords:

Induction melt thermoforming
Radiography
Mechanical properties
Optical microscopy

ABSTRACT

Recently, a novel thermoforming process involving induction heating of tin interlayers to create 'lubricated blanks' using low viscosity molten tin was demonstrated ("iMelt") (Harrison et al., 2020). Important to the success of the method is expulsion of the tin interlayer from the blank using a multi-step thermoforming operation. Approaches to characterise the quantity of residual tin and impact on the mechanical properties of the formed parts are established. 3D x-ray CT was used to accurately determine residual tin content while results from 2D x-ray scanning were shown to be highly-correlated with the 3D data and therefore can be a faster, low-cost alternative. After gradual refinement of the process, it was shown that residual tin volumes as low as 1.6 % were achievable in flat laminates. Compared to reference samples consolidated without tin, the remnant tin caused a reduction in yield strength and flexural stiffness, while producing comparable ultimate interlaminar shear strength.

1. Introduction

Thermoforming of continuous fibre thermoplastic composite laminates offers an avenue for rapid manufacture of high performance (lightweight, tough, corrosion resistant) structural components. Regulatory requirements such as the need to reduce emissions in transport and recyclability [1] are driving adoption, however there are several issues that continue to restrict their widespread use including various manufacturing issues [2]. Forming of wrinkle-free biaxial sheets is relatively simple [3–6], while forming of multiaxial sheets is much more challenging; the ply configuration in multiaxial sheets can lead to large inter-ply stresses between adjacent, but non orthogonal plies [7–9]. These additional stresses can lead to wrinkling when forming doubly curved geometries and these wrinkles can significantly reduce final part strength by up to 70 % [10,11]. One previously suggested solution to this problem has involved the insertion of thin thermoplastic polymer sheets into a layup to effectively lubricate the blank during the forming process [12]. The addition of low viscosity polypropylene interlayers to a glass-polypropylene matrix has been shown to increase maximum shear angle without wrinkling from $\sim 5^\circ$ to around $\sim 20^\circ$. However, the presence of a 1.5 mm interlayer lowered the fibre volume fraction to 14 % when compared to a 35 % fibre volume fraction with no interlayer [12]. The effectiveness of the lubricating polymer interlayer in this

method is also limited by the relatively high viscosity of molten thermoplastic polymers (~ 1000 Pas) which can still generate significant inter-ply friction during forming.

Recently, an alternative 'lubricated blank' approach was demonstrated [13] where molten metal (tin), which has a significantly lower viscosity than thermoplastic polymers (~ 2 mPas [14]) was used as the inter-ply lubricant during the press forming of pre-consolidated carbon fibre reinforced nylon advanced composites. This process will be referred to as iMelt forming in the rest of the paper. A layup of tin and carbon fibre reinforced nylon sheets was placed in a double diaphragm arrangement, a vacuum was drawn and the layup was internally heated using electromagnetic induction. A bespoke multistep tool was then used to press-form the blank. By beginning the forming process at the centre and progressively moving outwards towards the perimeter of the sheet, a pressure-driven squeeze flow is created, pushing the tin out of the blank during the forming process. As well as reducing friction during forming, the molten metal can provide homogeneous internal heating of the part. The manufacturing process produced good preliminary results, creating reasonably well thermoformed prototype parts. However, the success of the method depends on effective expulsion of almost all of the tin during forming; if even small quantities remain, then the mechanical properties of the formed part are likely to be lower and the average density of the formed composite part is higher. If the process is to

^{*} Corresponding author.

E-mail address: i.campbell.3@research.gla.ac.uk (I. Campbell).

<https://doi.org/10.1016/j.compositesa.2022.107286>

Received 29 March 2022; Received in revised form 26 October 2022; Accepted 30 October 2022

Available online 3 November 2022

1359-835X/© 2022 The Authors. Published by Elsevier Ltd. This is an open access article under the CC BY license (<http://creativecommons.org/licenses/by/4.0/>).

become a viable process option, the amount of residual tin has to be lowered to very low levels and the influence of the latter on the final mechanical performance of the formed parts must be understood. This means that a practical and low-cost method of measuring the amount and distribution of residual tin in the formed parts is needed.

One way to investigate the amount of residual tin is to use radiography. As x-rays pass through material, energy is lost via absorption or scattering allowing for analysis of the internal structure [15]. X-ray intensity along a path can be found using the Lambert-Beer's law as follows [16]:

$$I_x = I_0 e^{-\mu x} \quad (1)$$

where I_x is x-ray intensity at depth x , I_0 is x-ray intensity and μ is the linear attenuation coefficient. Strictly, this is only valid for x-rays of a single energy and wavelength; however, it provides a good approximation of the behaviour of polychromatic beams. The linear attenuation coefficient is influenced by a number of factors and depends on the interaction of photo absorption effects, Rayleigh scattering and Compton scattering [17]. Contrast between relevant features is a key issue and is largely dependent upon differing linear attenuation coefficients of the constituent features. In this investigation, the aim is to identify tin embedded in a nylon-carbon fibre laminate. The approximate linear attenuation coefficients of 6 cm^{-1} for tin, 0.4 cm^{-1} for pure carbon [18] and 0.2 cm^{-1} for nylon [19] mean that full depth penetration of the nylon-carbon fibre sample is possible, and the tin provides excellent contrast with the carbon/nylon composite due to its significantly higher attenuation coefficient.

Conventional radiography involves passing high energy electromagnetic radiation (x-rays) through an object and on to a detector (e.g. film, phosphor plate or semiconductor for digital imaging), creating a 2D 'shadow' of the internal structure of the object [20]. This process can be used to image the residual tin quickly; however, there is a limit to the technique's measurement accuracy due to the lack of information on through-thickness location [21,22]. In contrast, x-ray computed tomography (x-ray CT) can be used to construct a 3D image of an object. X-ray images are collected from multiple angles and reconstructive algorithms are used to create full 3-d images [17]. While x-ray CT is primarily used in the medical field, it has also been used to image the internal structure of naturally occurring rocks [16], manufactured products [23] and also in visualising the meso- and micro-structure of polymer composites, allowing imaging of internal fibre architecture and damage, with a potential resolution of around $5\text{--}7 \mu\text{m}$ [24–28]. Use of optical measurements can be used to verify and calibrate these images. As powerful as the method is, it does have drawbacks: high resolution scans can only be performed on small volumes, the scanning and reconstruction process can be time consuming and the initial cost for the equipment is high [24].

Turning to the effect of the residual metal (tin) on mechanical properties, a concern is that the existence of residual tin at the ply interface could lower the inter-laminar shear strength (ILSS). Adhesion occurs through a variety of mechanisms such as mechanical interlocking, physical bonding (e.g. Van Der Waals interactions) and chemical bonding [29]. Bonding in nylon structures relies primarily upon hydrogen bonds between adjacent polymer chains [30]. These bonds are strong, and as such, their interruption by the presence of residual tin may reduce the strength of the interlaminar interface, weakening the part and leading to failure via interlaminar shear. Interlaminar shear strength can be characterised using test standards, e.g. ISO 14130 [31], and is a measure of resistance to shear induced delamination failure in laminated composites [32,33]. In this investigation, it is used to examine the effect of residual tin on the ILSS. Adhesive bond strength can be very sensitive to material composition at the surfaces of the bonded materials. For example, surface oxidation and phenoxy coatings on fibres can dramatically increase the interlaminar shear strength of nylon-carbon composites [34–36]. The presence of voids and sharp changes in fibre

density can also reduce the ILSS [37,38]. Indeed, interlaminar failure at the metal/composite interfaces in epoxy-aluminium/carbon fibre laminates has been demonstrated previously [39–42]. The authors are not aware of any investigations specifically into tin/nylon bonding, however some research has shown that tin/polymer bond strength is sensitive to the type of polymer used (e.g. polyurethane vs polyurethane acrylic) [43]. Understanding the influence of the residual interlaminar tin on the ILSS of carbon/nylon composites is an important goal of this investigation. For simplicity, the current investigation is limited to the case of flat laminates rather than thermoformed parts of complex geometry. This should be the easiest and simplest scenario to examine the influence of any residual tin following the iMelt process.

The structure of the remainder of this paper is as follows: in Section 2 a brief description of the manufacturing process used to make the samples is provided [13]. Section 3 describes the x-ray methods used in the investigation. The quantity of tin present following iMelt forming is analysed in detail using optical methods in addition to both 2D and 3D radiography. These techniques are developed and optimised specifically for this application and consideration is given to the question of how to best to undertake the measurements for different purposes (e.g. rapid low-cost quality control or slow and expensive high accuracy measurements etc.). Section 4 describes the methods used to ascertain the impact of residual tin on the mechanical properties of the laminates. Results from these experiments are shown in Section 4 and finally conclusions are presented in Section 6.

2. Materials and manufacturing

For this paper, a number of laminates were consolidated to produce flat specimens for mechanical testing and non-destructive characterisation. Sub-laminates were prepared from TenCate Cetex TC910 nylon 6 UD tape [44] in a [0/90]_s layup, consolidated together in a heated press under 5.9 bar at 270 °C. The tape had a thickness of 0.16 mm, a fibre volume fraction of 49 % and a polymer content by weight of 40 %. The recommended processing temperature for the laminates is 249–271 °C. During the consolidation process, laminates were held in a silicone rubber diaphragm bag under atmospheric pressure (Silex 60° Shore A Hardness High Temperature Silicone Rubber Sheet [45]). Four distinct carbon-nylon laminate types were then heated and consolidated together from the sub-laminates using the following protocols that relate to the type of heating and consolidation conditions and the presence (or not) of a tin interlayer:

1. **No Tin (Radiant):** Four [0/90]_s carbon-nylon sub-laminates in a [0/90/90/0/90/0/0/90]_s layup were heated under vacuum in a 0.3 mm thick silicone rubber diaphragm bag at 250 °C (without interlaminar tin) using a 5.7 kW radiant heater (Watlow Raymax 2030) before being shuttled across and further consolidated with the same multistep tooling described in [13], creating a total consolidation pressure of 2 Bar between the vacuum pressure and pressure from the forming tool. Temperature was monitored using a Flir E8-XT Infrared Camera and temperature was recorded at the upper diaphragm surface. The part was heated for 15 min, and after forming, was held in between the steel male and steel female tool to cool for 15 min. This laminate is used as a control for the impact of residual interlaminar tin.
2. **No Tin (Platens):** Four carbon-nylon sub-laminates were consolidated (without interlaminar tin) between electrically heated platens at 4 Bar and 270 °C. The platens were air cooled for 50 min to 150 °C before being water cooled for 10 min to room temperature. The overall layup was again [0/90/90/0/90/0/0/90]_s. The two 'No Tin' laminates serve as examples of conventional consolidation methods. This sample was used as an external control to validate our manufacturing process.
3. **Tin (Induction A):** Four sub-laminates of carbon-nylon composite were interspersed with three sheets of tin with a layup of [0/90/90/

0/T/90/0/0/90/ \bar{T}]_s. Here *T* indicates a tin interlayer. The layup was then heated via electromagnetic induction of the tin to ~ 250 °C under vacuum in a 0.3 mm thick silicone rubber diaphragm bag and consolidated using the multistep tool. Temperature was measured from the upper surface of the Silicone Diaphragm using an infrared camera. The part was consolidated between steel male tool and epoxy-glass fibre composite female tool for fifteen minutes. Further details on the induction assisted forming can be found in [13].

- 4. Tin (Induction B):** These specimens were prepared in the same way as Tin (Induction A), except with an additional 1 mm thick silicone rubber sheet inserted between the composite sample and the diaphragm bag. This change had a few benefits. It lowered heat flow through the diaphragm and out of the sample, increasing the relative significance of conduction within the matrix material and improving temperature homogeneity. It also acted to improve the structural integrity of the diaphragm to help it support the heavy molten tin, improving consistency of the heating process. Finally, it also acted to smooth over discontinuities in the pressure distribution at the edge of the rings of the multi-step press.

Following these steps, a number of samples were manufactured for mechanical testing: One of ‘No Tin (Radiant)’ and one of ‘No Tin (Platens)’. These are respectively referred to as ‘No Tin-R’ and ‘No Tin-P’ in future text and figures. Additionally, three samples of type ‘Tin (Induction A)’, and two samples of type ‘Tin (Induction B)’ were produced. These are denoted Tin-IA1 to Tin-IA3 and Tin-IB4 to Tin-IB5 in future text and figures. A larger number of tin samples were analysed to provide a larger number of data points allowing for more detailed exploration of the impact of residual tin. Table 1 summarises the conditions used in each of the four consolidation methods. A final point to note is the variable cooling conditions, particularly between ‘No Tin-P’ and the other methods. Slower cooling rate has been shown to lead to higher crystallinity [46] in finished samples, and as a result may lead to high interlaminar fracture toughness [47,48].

3. Optical and radiographic analysis

The quantity and distribution of residual tin in the post-consolidated laminates, was measured using three techniques: 2D x-rays, 3D x-ray CT and optical imaging of the cross-section. For 2D x-ray analysis, samples were scanned at 130 kV and 5 mA for 2 s from a distance of 600 mm using an x-ray generator. The images were collected on D4 film and digitised using a backlight and digital camera. For 3D x-ray analysis, selected samples were further scanned in a Nikon XT H 225/320 LC computed tomography device at 140 kV and 136 μA energy. A 0.5 mm tin pre-filter was placed over the tube to reduce the impact of beam

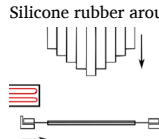
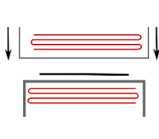
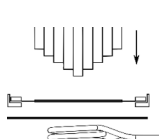
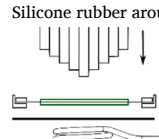
hardening effects [49]. A voxel size of approximately 60 μm was achieved for all samples. The CT scan data was compared with polished cross-sections to ensure accurate thresholding values were chosen. For the sectioning, samples were bisected, mounted in resin and polished using a Struers LaboForce-50. Images were then captured using a Thorlabs Cerna optical microscope with 8-megapixel digital camera and a x5 lens. The sample was mounted on a motorised stage and images were taken to cover the full sample. The images were then stitched together using Hugin Panorama photo stitching software.

We hypothesise that the impact of the tin on final material properties may correlate with either (1) the percentage projected surface area which is covered by residual tin, or (2) the percentage volume of residual tin in a part. The first metric gives an indication of the interrupted interlaminar bonding between plies. The second provides an estimate of the mass of residual tin within the laminate, without information on the distribution of the tin within the laminate. To quantify these metrics, the CT scan data was first thresholded in Simpleware ScanIP (Synopsis, USA) to identify regions of tin. The scan was then exported into a 3D image stack and analysed in MATLAB. Surface area characterisation was obtained by projecting the full image stack onto a single plane and then calculating the areal tin coverage using the known voxel dimensions. Volume characterisation used a similar method, however a count was kept to determine the “thickness” of each superimposed pixel. This approximated thickness was then used to calculate the total volume of residual tin.

4. Mechanical testing

Interlaminar Shear Strength tests were carried out in a three-point bending fixture in accordance with ISO 14130. The test specimens had thickness, *t*, ranging from 1.9 – 2.67 mm, and as such, test specimens of length *L* = 20 mm and breadth 10 mm were prepared. The test was carried out in a Deben Microtester (Deben, UK) with a 5 kN loadcell. The test setup is shown in Fig. 1. A loading plunger (a) with radius 5 mm is used to apply force at the mid-span. The specimen (b) is mounted on two supporting bars (c) of radius 2 mm. The span, *s*, of the support was set to 12.5 mm. The flexural properties of the specimens is influenced by the relative orientation of the layup to the long axis of the specimen, as such two test types specimen were prepared: one with the outer fibres parallel to the long axis of the specimen (Orientation 1) and the other having the outer fibres perpendicular to the axis of the specimen (Orientation 2). The rectangular specimens were carefully cut out from the formed discs using a diamond coated rodsaw before being filed to size. The location of each cut specimen was recorded to enable accurate cross referencing with the CT scans. This allowed for estimation of the residual tin content specific to each of the ILS samples. Specimens from the four

Table 1
Details of the forming processes.

	1. No Tin-R	2. No Tin-P	3. Tin-IA	4. Tin-IB
Consolidation Temp (°C)	270	270	250	250
Consolidation Pressure (Bar)	2	4	2	2
Heating Method	Radiant Heater	Heated Platens	Induction Heater	Induction Heater
Cooling Method	15 min. consolidation in press	50 min. air cooling > 10 min. water cooling	15 min. consolidation in press	15 min. consolidation in press
Layup	[0/90/90/0/90/0/0/90] _s	[0/90/90/0/90/0/0/90] _s	[0/90/90/0/T/90/0/0/90/ \bar{T}] _s	[0/90/90/0/T/90/0/0/90/ \bar{T}] _s
Consolidation Tool	Multi-Step Press + Steel Base	Heated Platens	Multi-Step Press + Epoxy-glass fibre base	Multi-Step Press + epoxy glass fibre base
Diaphragm	0.3 mm Silicone Rubber + 1.0 mm thick Silicone rubber around layup	n/a	0.3 mm Silicone Rubber	0.3 mm Silicone Rubber + 1.0 mm thick Silicone rubber around layup
Diagrammatic representation (Not to scale)				

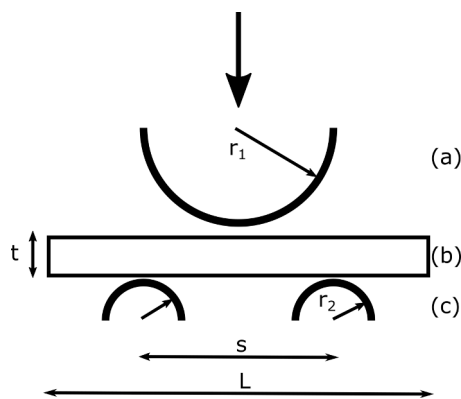


Fig. 1. Schematic of ILS test setup. (a) loading cylinder with radius $r_1 = 5$ mm (b) specimen of approximate dimension $20 \times 10 \times 2$ mm and (c) support cylinders of radius $r_2 = 2$ mm and span $s = 12.5$ mm.

manufacturing processes described in Table 1 were tested. The key mechanical properties (ILSS and Yield Strength) were then determined from the force–displacement curves.

Interlaminar shear stress was calculated via the following equation in accordance with ISO 14130.

$$\text{Interlaminar shear stress} = 0.75 \frac{P}{bt} \quad (2)$$

Where P is the applied plunger force, b is specimen width and t is specimen thickness. Both the maximum value (i.e. interlaminar shear strength, ILSS) and its yield value (ILSS_Y) were considered. Interlaminar shear strength was defined in accordance with ASTM D2344 via the maximum force reached when any one of the following conditions were met: (a) two piece specimen failure, (b) a force drop-off of 20 % or (c), 1.8 mm of plunger displacement was reached. 1.8 mm was chosen as, beyond this point, the specimen begins to be compressed between the plunger and the supporting bars, causing a rapid increase in the applied load. As there was considerable variation in the specimens and the force–displacement plots, yield was defined by either a 0.2 % yield offset or by a drop in force (whichever occurs first). The yield stress was similarly calculated using Eq. (2).

5. Results and discussion

5.1. Radiographic and optical analysis of residual tin content

In this section, an overview of the x-ray and optical analysis of the residual tin content is given. Table 2 shows the percentage volume of residual tin and the percentage volume of tin expelled during consolidation in the five samples containing tin (each one for the entire formed disc). Over the duration of the investigation [13], the iMelt process was steadily improved, this is apparent in the results presented

Table 2
Residual tin volume as a percentage of final part volume for parts Tin-IA1-IA3 and Tin-IB4-IB5, determined using CT scans.

Test	Residual Tin Volume (%)	Volume of Original Tin Interlayer Removed (%)
Tin-IA1	$5.7 \pm_{2.6}^{4.1}$	$97.0 \pm_{1.4}^{2.1}$
Tin-IA2	$4.2 \pm_{1.6}^{2.4}$	$97.8 \pm_{0.9}^{1.3}$
Tin-IA3	$1.5 \pm_{0.5}^{0.8}$	$99.4 \pm_{0.4}^{0.2}$
Tin-IB4	$2.5 \pm_{1.3}^{2.2}$	$98.6 \pm_{1.3}^{0.8}$
Tin-IB5	$1.6 \pm_{0.9}^{1.6}$	$99.0 \pm_{0.9}^{0.5}$

chronologically from top to bottom in Table 2: i.e. residual tin quantities decrease as the process was improved over time.

The microscope images of the polished cross section in Fig. 2. show that the residual tin lies almost exclusively in the three interfaces corresponding to the original tin sheet locations. It can also be seen from the images that the residual tin tends to form large fragments with the vast majority being above $100 \mu\text{m}$. This indicates that the CT scans will detect the vast majority of the residual tin inside the sample and can be used to give an accurate representation of the level of residual tin.

Fig. 3 shows a comparison between a 3D CT scan and a 2D film X-ray of a bisected sample. Fig. 3a shows the raw segmented data from the CT scan with a significant number of residual tin fragments distributed around the specimen. In Fig. 3b this data has been transformed in MATLAB to produce a 2D projection with light intensity scaling with thickness of tin. Fig. 3b indicates that the majority of the residual tin is, in fact, quite thin as can be seen from the dark grayscale values when the thickness is taken into account. Finally, in Fig. 3c a digitised 2D film x-ray of the same sample is shown. In this instance, it is clear that both methods capture similar physical phenomena, although the CT scan has higher resolution and is able to detect smaller fragments than the 2D x-ray.

The importance of the 2D x-ray lies in the speed that it can be deployed in the quality control of parts, although less accurate in detecting smaller fragments. The images in Fig. 3, which contains a sample with a relatively high volume of tin, indicates that the 2D film x-ray may be sufficient to rapidly assess the quality of mass-produced parts in the hands of experienced users.

Analysis of the samples was carried out in MATLAB (see Section 3) to calculate the total tin volume and the total projected surface area covered by tin, for a selection of smaller samples. In total, 64 samples with interlaminar tin and dimensions 20×10 mm were examined and later tested mechanically using the interlaminar shear test. The volume versus projected surface area of residual tin within each test piece is plotted in Fig. 4. A high level of correlation is apparent ($r^2 = 0.92$), suggesting that the lateral projected surface area of residual tin is roughly proportional to its volume.

The strong correlation between projected surface area and volume of residual tin indicates again that the simpler 2D x-ray approach may be sufficient to make judgement calls on residual tin content. To test this possibility, a comparison between the projected surface area from the CT scan and the calculated surface area of tin from the 2D film x-rays was made. Film x-rays (captured and digitised as detailed in Section 3) were thresholded via the Renyi Entropy thresholding algorithm [50] in ImageJ. These thresholded images were then analysed via MATLAB to

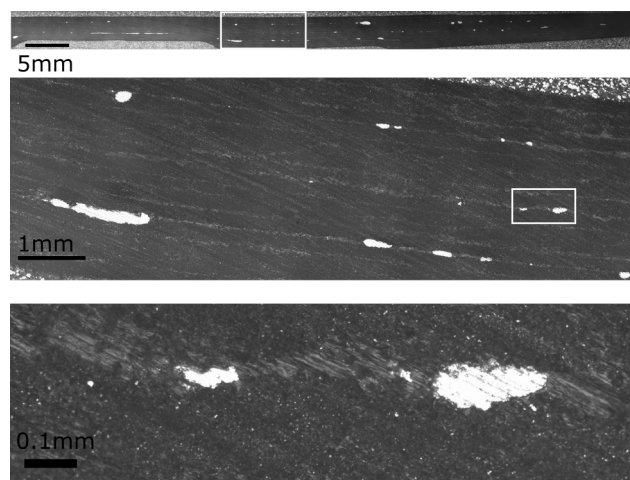


Fig. 2. Microscope images of the polished cross section. Images taken from sample Tin-IA3. Lines indicate the 3 interlaminar layers which originally contained interlaminar tin.

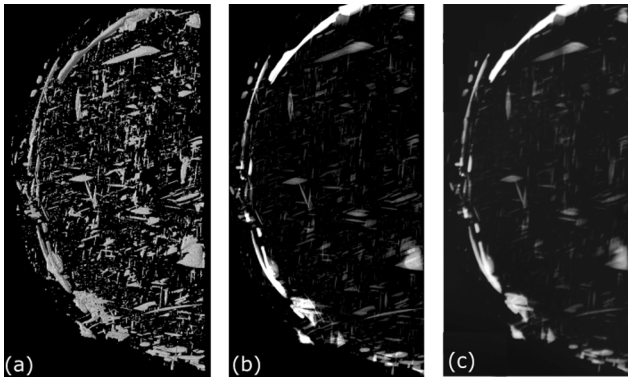


Fig. 3. Comparison between (a) segmented 3D CT scan showing residual tin in a bisected circular sample (b) 2D projection of same 3D scan with intensity adjusted for thickness and (c) 2D X-ray of same sample. Results are from the Tin -IA1 sample (containing ~ 5.7 % vol of tin).

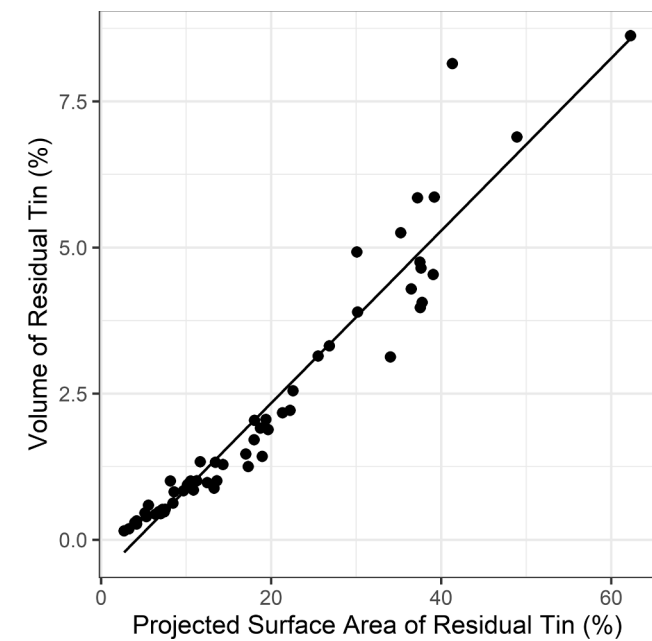


Fig. 4. Volume of residual tin versus projected surface area, measured using 3D x-ray CT.

establish the surface area (projected) of residual tin in the samples. A comparison between the surface area percentage as calculated from the x-ray CT scans with that calculated from the film x-rays is shown in Fig. 5. The dashed line represents a 1:1 relationship. The plotted data suggest that the CT scans tend to give a higher value than the 2D film x-rays, however this tendency fades at higher quantities. It is therefore plausible that smaller fragments of residual tin are missed by the lower resolution 2D film x-rays and a higher resolution system may be required to fully match the x-ray CT scans.

A final point regarding the quantity of residual tin is its influence on average density. Tin is significantly denser than nylon. The percentage change in density ($\%_{\Delta\rho}$) when a volume of tin (V_t) replaces an equivalent volume of CFR nylon from a part with original volume (V_o) can be found as follows,

$$\%_{\Delta\rho} = \frac{[\rho_{nylon}(V_o - V_t) + \rho_{tin}(V_t)] - (V_o) \times \rho_{nylon}}{V_o \times \rho_{nylon}} \quad (3)$$

Taking $\rho_{nylon} = 1.45 \text{ g/cm}^3$ and $\rho_{tin} = 7.28 \text{ g/cm}^3$ gives the following:

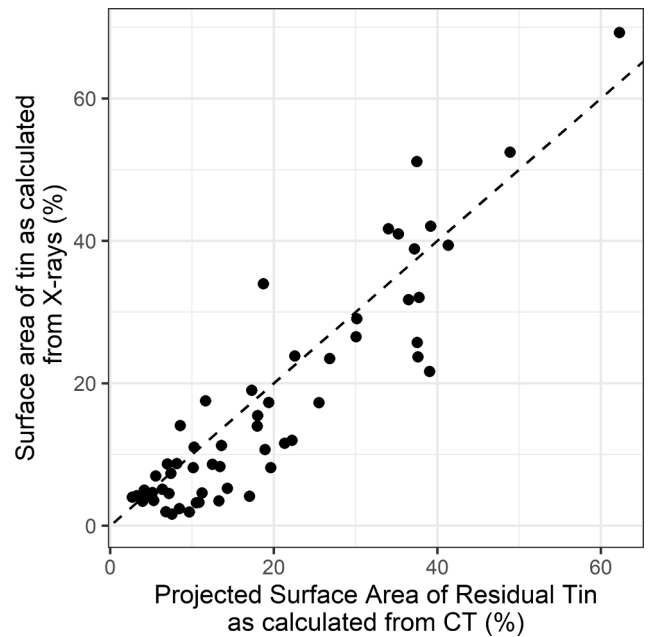


Fig. 5. Comparison between surface area calculated via film x-rays and projected surface area calculated via the 3D CT scans. Dashed line represents 1:1 relationship. The film x-rays underpredict the surface area of each analysed fragment.

$$\%_{\Delta\rho} = \frac{\rho_{tin} - \rho_{nylon}}{\rho_{nylon}} \times \frac{V_t}{V_o} = > 4.02 \frac{V_t}{V_o} \quad (4)$$

Alternatively, comparing the density of the tin with the density of the composite sheet as a whole ($\rho_{CFRnylon} = 1.73 \text{ g/cm}^3$ [45]) gives.

$$\%_{\Delta\rho} = \frac{\rho_{tin} - \rho_{CFRnylon}}{\rho_{CFRnylon}} \times \frac{V_t}{V_o} = 3.2 \frac{V_t}{V_o} \quad (5)$$

This shows that the density of a composite with one percent of tin by volume would be ~ 3–4 percent denser than without the tin, and five percent of tin by volume would be ~ 15–20 percent denser. This clearly necessitates minimising tin content for the process to be viable.

5.2. Effect of heating and consolidation method on mechanical properties

Table 3 shows the breakdown of the tested specimens based on forming method, orientation and part dimensions. A total of 96 specimens were tested. Orientation 1 has the outer fibres parallel to the long axis of the part, and Orientation 2 has the outer fibres perpendicular to the long axis.

The graphs in Fig. 6 show the running mean of the deflection versus ILSS curves for each manufacturing method allowing the reader to better appreciate the nature of the failure of samples produced by the different production methods. Each graph shows average results, for both relative orientations, indicated by the continuous and dashed lines. The range of results (highest to lowest measurement) is shown by the lighter shade colour, and all individual curves are plotted in the bottom right. Looking at the range (shaded region) in the plots of Fig. 6, the laminates without tin clearly show less scatter. Finally, it can be seen that all specimens, except for 'No Tin-P', exhibit gradual plastic failure. As the crosshead displacement increased, these relatively ductile specimens were bent to such a degree that they were eventually compressed between the plunger and the two support bars, at which point the results become invalid. This occurs at a displacement ~ 1.8 mm; consequently all results shown in Fig. 6 have been truncated accordingly.

Table 4 shows the P-values of a Welch Two Sample T-test used to evaluate the impact that specimen orientation had on the results. The

Table 3
Detailed dimensions of interlaminar shear specimens by forming method and orientation. In Orientation 1, the outer fibres are parallel to the long axis of the sample. In Orientation 2, they are perpendicular to the long axis of the sample.

Forming Method	Orientation	No. Samples Tested	Thickness (mm)	Length (mm)	Breadth (mm)
No Tin-R	1	6	2.08 ± 0.04	19.90 ± 0.25	10.08 ± 0.19
No Tin-R	2	6	2.06 ± 0.07	19.87 ± 0.13	9.94 ± 0.13
No Tin-P	1	6	2.30 ± 0.05	19.72 ± 0.39	9.98 ± 0.17
No Tin-P	2	6	2.32 ± 0.06	19.88 ± 0.25	9.90 ± 0.09
Tin-IA1	1	7	2.42 ± 0.08	20.18 ± 0.26	10.02 ± 0.12
Tin-IA1	2	9	2.42 ± 0.11	19.91 ± 0.41	10.03 ± 0.10
Tin-IA2	1	7	2.36 ± 0.07	20.09 ± 0.54	10.13 ± 0.09
Tin-IA2	2	8	2.35 ± 0.08	19.91 ± 0.53	10.10 ± 0.10
Tin-IA3	1	7	2.27 ± 0.13	19.78 ± 0.34	10.06 ± 0.20
Tin-IA3	2	8	2.28 ± 0.30	20.17 ± 0.36	9.96 ± 0.11
Tin-IB4	1	7	2.48 ± 0.17	20.12 ± 0.29	10.46 ± 0.37
Tin-IB4	2	7	2.37 ± 0.18	20.25 ± 0.48	10.49 ± 1.0
Tin-IB5	1	6	2.48 ± 0.15	20.27 ± 0.61	9.99 ± 0.32
Tin-IB5	2	6	2.34 ± 0.18	20.11 ± 0.31	10.18 ± 0.27

high P-values (>0.05) suggest that the impact of orientation is not significant on the measured material properties. This is likely due to the high number of plies (16) in the samples reducing the relative contribution of any single ply. For completeness we will continue to show results for each orientation separately.

Fig. 7 shows Interlaminar shear stress versus crosshead displacement (deflection) for one representative ‘No Tin-R’ specimen. Inset photos show the progression of deformation and failure corresponding to points (A to D) on the loading curve. The sample initially begins to deform

plastically (B) before visible delamination occurs in the midplane, roughly half-way between the applied loading and the support cylinders - i.e. corresponding to the locations of maximum shear stress in three-point bending. In Fig. 8, results for a representative specimen having relatively high residual tin content (~21 % surface area, from ‘Tin-A2’) is shown. The specimen fails via delamination occurring close to an agglomeration of residual tin, as shown in (C). This is again close to the location of maximum shear stress, so the presence of tin appears to have weakened the specimen and eventually leads to tensile failure of the part in (D). In Fig. 9, results for another representative specimen containing rather less residual tin (~6.8 % surface area, from ‘Tin-A3’) is shown. In this case, the initial visible delamination occurs between the loading cylinder and the support cylinder, but appears in the bottom half of the laminate (highlighted in C). The propagation of this delamination is limited and the sample primarily experiences plastic deformation. For most examples, failure tended to initiate around the midpoint between the loading and supporting cylinder. This corresponds with the location of maximum shear stress in the three-point bending arrangement (Makeev et al. [51]).

In some cases, the presence of tin leads to weakening of the inter-ply interface and more rapid delamination. However, it also appears that the presence of the tin, in some cases, leads to a more ductile response where the tin tends to improve the ability of the beam to absorb energy via accommodation of further bending rather than by propagation of cracks to sudden failure. This is clearly seen in the example shown in Fig. 9. Interlaminar veils have been used with varied success to improve resistance to fracture and improve ductility within composites [52–54].

Table 4
Statistical impact of the orientation of the tested sample on the mechanical properties of the sample. Welch Two Sample T-test was used. P-values are shown. Orientation shows no statistically significant impact on mechanical properties. In Orientation 1, the outer fibres are parallel to the long axis of the sample. In Orientation 2, they are perpendicular to the long axis of the sample.

	P-value ILSS	P-value ILSS _y
No Tin-R	0.73	0.06
No Tin-P	0.22	0.68
Tin-IA	0.79	0.28
Tin-IB	0.12	0.12

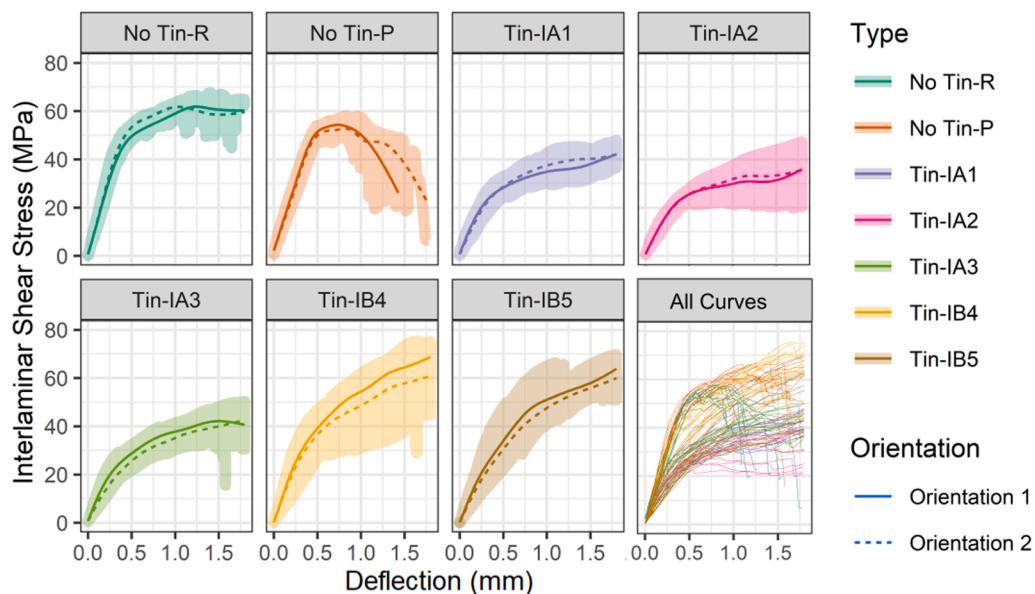


Fig. 6. Mean interlaminar shear stress versus deflection for each specimen type and orientation. The range of the results is indicated by the faded background. The bottom right plot shows all individual curves.

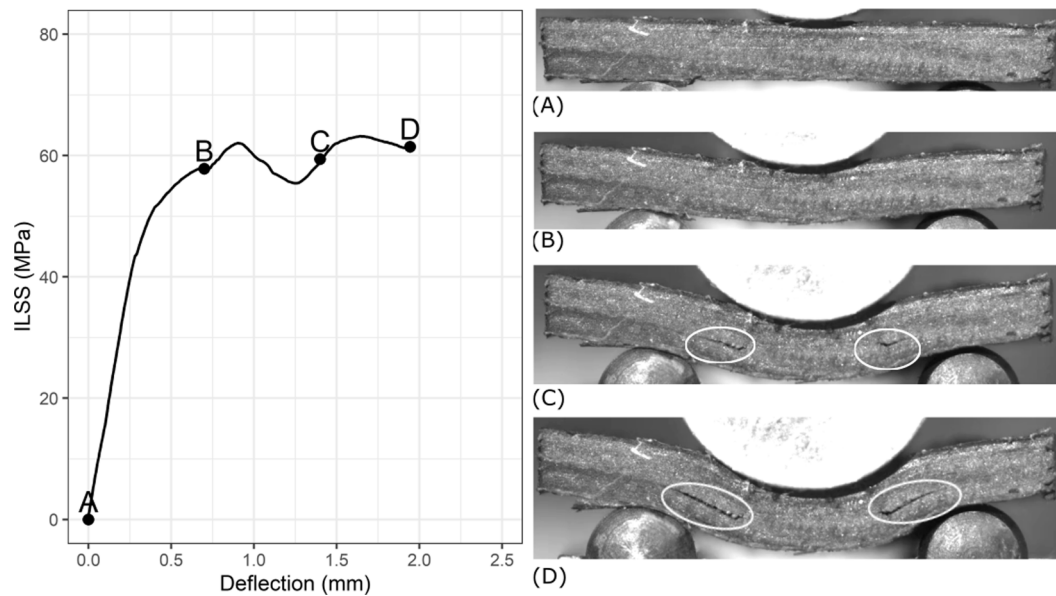


Fig. 7. Interlaminar shear stress versus deflection for a selected ‘No Tin-R’ radiant heated specimen. Inset photos show the progression of deformation and failure corresponding to points (A to D) on the loading curve. The circled areas indicate regions of shear-induced delamination corresponding to the locations of maximum shear stress.

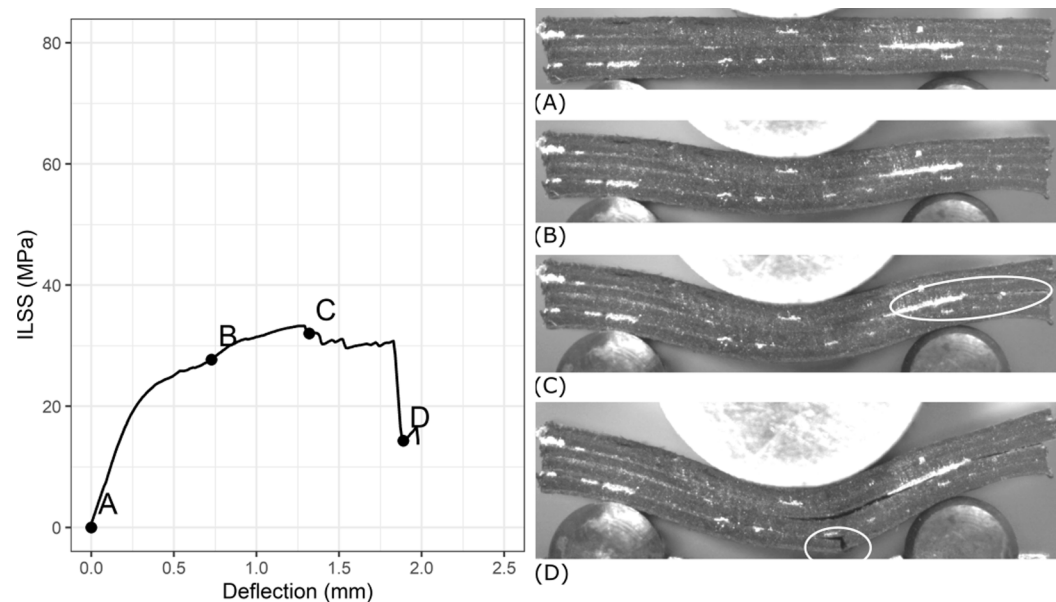


Fig. 8. Interlaminar shear stress versus deflection for a selected sample containing high quantities of residual tin (from disc ‘Tin-IA2’). Inset photos show the progression of deformation and failure corresponding to points (A to D) on the loading curve. Failure initiates near the location of high tin content which also corresponds roughly with the location of the maximum shear stress in (C). Further cracking is apparent later in (D) due to tensile bending stress. Stress-deflection plot shows a sudden ‘brittle like’ failure.

One of the mechanisms is the deflection of crack growth towards longer and harder paths, increasing energy required for crack propagation [55]. Residual tin fragments may mimic this behaviour by deflecting crack growth and absorbing energy through ductile deformation. This behaviour will require closer examination as factors such as size of inclusion and coatings have a strong influence on the final behaviour in interlaminar veils and are likely to also impact behaviour of interlaminar tin [54,56].

Fig. 10 shows the mean interlaminar shear strength of the tested specimens. In the case of the samples without tin (i.e. ‘No Tin-R’ & ‘No Tin-P’), platen heated and consolidated samples (‘No Tin-P’) show lower ILSS than those heated and consolidated with the radiant heater and

multi-step tool (‘No Tin-R’). As discussed in Section 2, slower cooling rate (‘No Tin-P’) has been shown to lead to lower interlaminar fracture toughness [47,48] which agrees with these results. For samples heated and consolidated via induction heating and the multi-step tool (with tin present), ‘Tin-IA’ samples show a significantly lower strength than the ‘No Tin’ cases, whereas ‘Tin-IB’ samples had comparable values. As mentioned, ‘Tin-IA’ & ‘Tin-IB’ samples are similar, except for an additional 1 mm thick silicone rubber sheet inserted between the sample and the diaphragm bag in ‘Tin-IB’ samples (see Section 2). The changes in resultant heating and cooling patterns appears to have led to improvements in mechanical performance of the resulting specimens. This combined with the improved tin expulsion by smoothing over pressure

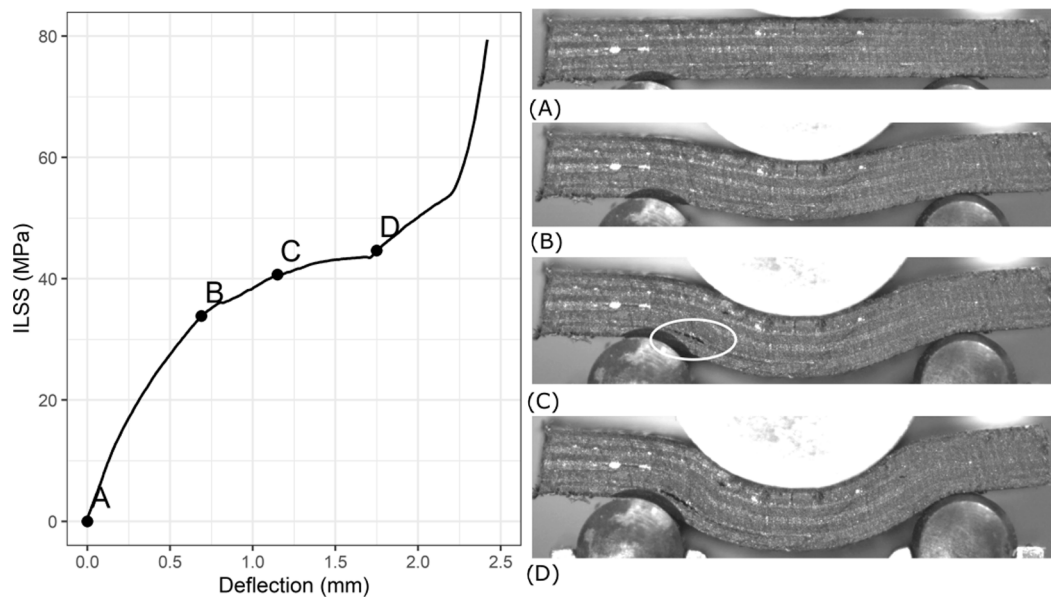


Fig. 9. Interlaminar shear stress versus deflection for a selected sample containing relatively lower quantities of residual tin (from disc ‘Tin-IA3’). Inset photos show the progression of deformation and failure corresponding to points (A to D) on the loading curve. In this sample, delamination has occurred near the cross-section of maximum shear stress. Stress-deflection plot shows a ‘ductile-like’ response such that there is no sudden failure and the sample deforms until it gets compressed between plunger and support bars after Point (D).

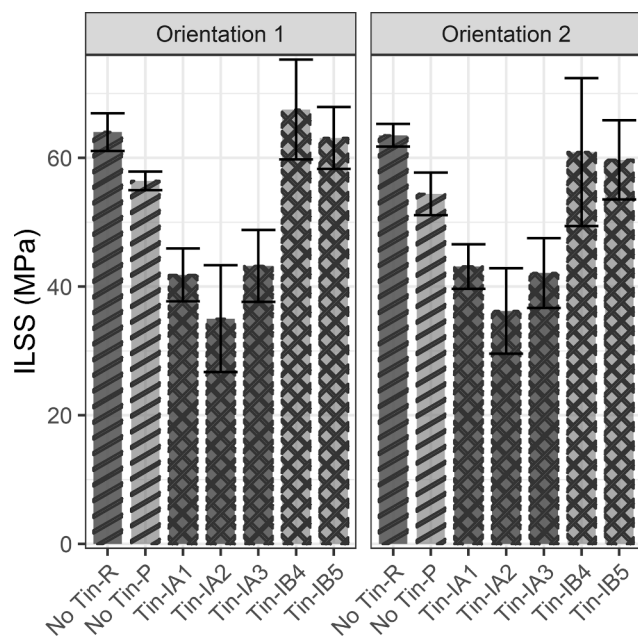


Fig. 10. Interlaminar Shear Strength (ILSS) by sample and orientation. Error bars show standard deviation of results.

discontinuities may have mitigated the formation of localised agglomerations of tin in the samples during consolidation (see Table 2). All the specimens that used tin interlayers (‘Tin-IA’ & ‘Tin-IB’) show higher variability than the samples without tin interlayers, probably due to the stochastic nature of residual tin coverage within the consolidated samples. The fact that the ILSS of the ‘Tin-IB’ samples have statistically insignificant differences with the ‘No Tin-R’ & ‘No Tin-P’ samples is encouraging and shows that simple, and not always obvious, changes to the setup can significantly improve the process (though the exact mechanism for this improvement is not yet fully understood).

The mean interlaminar shear stress at yield is shown in Fig. 11. The results here are less positive for the samples manufactured using the

iMelt process. Specimens with a tin interlayer (‘Tin-IA’ & ‘Tin-IB’) both show significant reductions compared to the ‘No Tin’ samples, though the reduction for ‘Tin-IB’ is notably less than that of ‘Tin-IA’, again suggesting that changes to the process can lead to notable improvements, this time for the interlaminar shear yield stress. It is probable that the presence of interlayer tin initiates earlier onset of shear induced delamination owing to a reduction in the adhesive bond strength of the inter-ply interface. Why this occurs for Yield strength and not maximum strength is unclear.

Table 5 shows the average thicknesses and mechanical properties by sample type, with the percentage difference compared with the control ‘No Tin-R’ specimens marked in brackets. The specimens manufactured

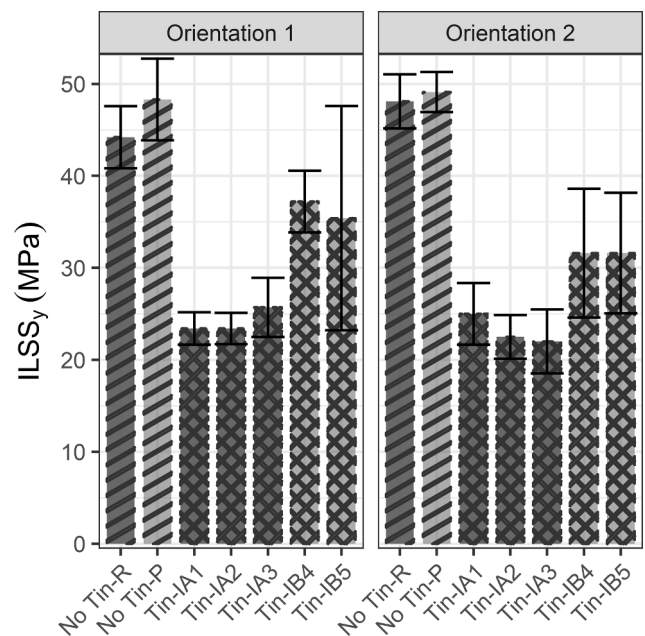


Fig. 11. Interlaminar shear stress at yield (ILSS_y) by sample and orientation. Error bars show standard deviation of results.

Table 5

Overall mean thickness and mechanical properties for the interlaminar shear results. Percentage change from the radiant samples (as a reference) is shown in brackets.

	Thickness (mm)	ILSS (MPa)	Yield Strength (MPa)
No Tin-R	2.31	63.7	46.1
No Tin-P	2.07 (-10.1 %)	55.4 (-13.1 %)	48.7 (+5.5 %)
Tin-IA	2.35 (+1.9 %)	40.3 (-36.7 %)	23.7 (-48.7 %)
Tin-IB	2.42 (+4.9 %)	62.9 (-1.3 %)	34.0 (-26.4 %)

with the multistep tooling are 11.5 to 16.9 % thicker than those produced with the heated platens, 'No Tin-P'. This is primarily because the edges of the platen formed samples were unconstrained during forming leading to some degree of transverse squeeze flow and mass-loss out the side of the sample during consolidation [57].

The maximum measured ILSS (63.7 MPa) occurs in the radiant heated 'No Tin-R' control specimens. 'Tin-IA' is significantly lower than this, at just 40.3 MPa, though 'Tin-IB' has a similar strength of 62.9 MPa. This difference in the performance of Tin-IA and Tin-IB specimens has a few potential explanations: (1) improved temperature/pressure conditions as a result of improved operator control of the heating process

(specifically, slowing down the heating rate and adjusting the induction coil to address cold spots) and the addition of extra silicone rubber layers around the sample, (2) the presence of a thin scattered layer of residual tin may act to distribute shear stresses away from the midplane location of maximum shear [51]. The Yield Strength of the 'Tin-IA' specimens is 48.7 % lower than the No Tin-R Specimens. The Yield Strength of the 'Tin-IB' specimens is also lower than the 'No Tin-R' specimens by 26.4 %, and is therefore an improvement in performance compared to the 'Tin-IA' specimens.

5.3. Impact of tin content on mechanical properties

To better understand the sensitivity of various parameters on the mechanical properties of the consolidated specimens, Fig. 12 shows a matrix of the full test results produced using 'Tin-IA' and 'Tin-IB'. Viewing the data in this way allows a granular analysis of the entire dataset of results produced using the iMelt heating and consolidation process. The matrix allows direct comparison between each of the following parameters: tin surface area coverage, specimen thickness and the mechanical properties (ILSS, ILSSy & Flexural Modulus). The axes related to each plot can be found by referring to the end of the row and

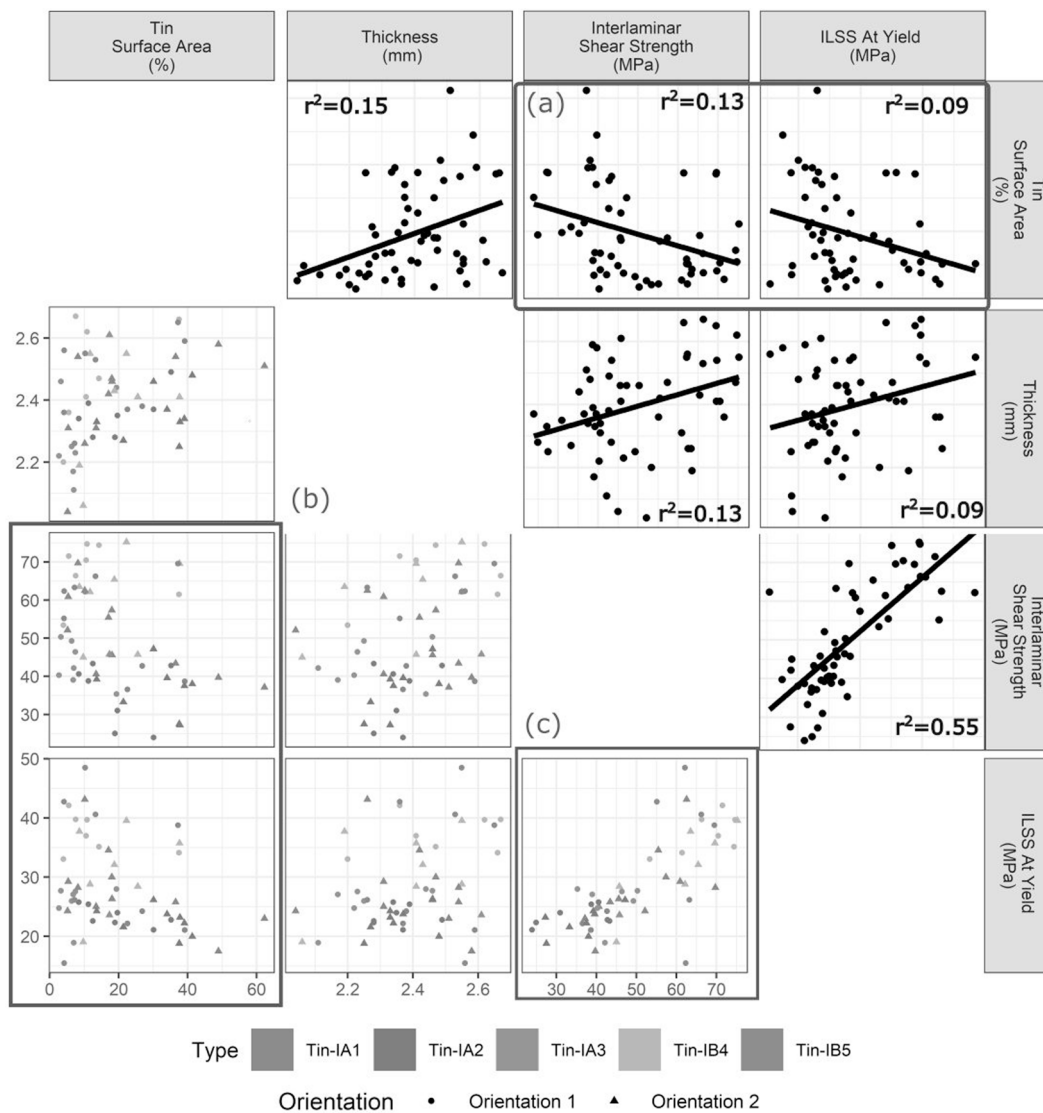


Fig. 12. Pair plots of the full set of results obtained from the tested tin based specimens: Top right shows linear regression + adjusted r^2 value over all results. Bottom left shows results segregated by sample type: (a) tin surface area vs mechanical properties, (b) tin surface area vs mechanical properties by sample and (c) relationship between ILSS and Yield Strength.

column occupied by the plot. The colours in the legend represent the various discs, 'Tin-IA1' to 'Tin-IA3' and 'Tin-IB4' to 'Tin-IB5', from which mechanical test specimens were cut. The figures on the top right show linear regressions carried out on the full dataset, along with r^2 values. Table 6 shows p-values for the significance of the correlation between tin surface area cover and the mechanical properties for the overall dataset (all samples taken together) and for the datasets separated by sample.

There is a statistically significant (all p-values < 0.05) negative correlation between surface area and the measured mechanical properties when looking at all samples together (see Fig. 12a). This correlation is quite weak with r^2 values of 0.13, 0.09 and 0.10, respectively. The significance of this correlation disappears when the results are separated by sample as seen by the high p-values in Table 6 (See also, Fig. 12b). As might be expected, there is a correlation between the ILSS and the ILL_{S_y} of the tested specimens ($r^2 = 0.55$). It is also possible to see clustering of results by manufactured samples (Fig. 12c). Given the weak correlations found between tin content and mechanical properties, and no correlation within single manufactured samples, it appears that variation in a manufactured sample's processing conditions continues to have an impact on the final properties. The difficulty in optimising the induction heating of a molten tin interlayer led to variation in forming temperatures within the sample and between samples. In addition to this, the addition of extra silicone rubber sheets around the samples for 'Tin-IB4' and 'Tin-IB5' will have smoothed over pressure discontinuities from the multistep tool as applied on the sample during forming and also will have changed the cooling rate after forming.

The experiments were designed to assess the impact of the residual tin on the mechanical properties of the produced part. There was a significant differences between manufactured samples, and a weak negative correlation between tin quantity and mechanical properties when all results were considered together. However, there was no evidence of any direct correlation between mechanical properties and tin content within manufactured samples (See Table 6). Some possible reasons for this are: (1) the distribution of the tin within the sample is likely to have an impact and this may be more significant than simply the quantity, (2) the marginal impact of additional tin may be smaller than the impact of variable conditions between samples such as temperature, pressure and cooling rates. These factors are widely acknowledged to be crucial in determining material properties of composites [47]. During the work, the induction heating process was in development, and as such, there is likely to be significant scope to improve repeatability. For example, we have shown that the addition of the extra silicone rubber protection in the 'Tin-IB' samples led to lower tin content and higher ILSS and yield strength.

The results obtained with the 'Tin-IB' samples (i.e. after refinement of the process) are encouraging for the method. Interlaminar shear strength for these samples was comparable with the 'no tin' (platen heated) samples. A number of tin based specimens responded similarly to Fig. 9 where significant bending deformation occurred without any drop-off in loading. This suggests that the tin may play a role in

increasing energy absorption by facilitating further deformation of the samples as opposed to sudden failure by detrimental propagation of cracks. Unfortunately, work to failure could not be reliably evaluated in the experiments as many of the specimens were sufficiently ductile to deform in bending until being compressed between the loading plunger and the support pins without showing any drop-off in load (see Fig. 9).

6. Conclusions

The concept of using metal interlayers to achieve low friction induction melt thermoforming of composite parts (iMelt) was proposed recently by the present authors in Harrison et al. [13]. The metal (in this case tin) facilitates the induction heating of the part and, when molten, enables very low friction in forming due to its low viscosity. This helps to reduce wrinkles and defects in the final part. A multi-step forming approach (moving outward from the centre) was used in Harrison et al. to execute the forming, but also to try to evacuate the tin from the final part. This paper addresses the critical next question; namely, how to characterise how much tin is present in the final part and how to evaluate its impact on mechanical properties?

The present paper outlines how 2D x-ray and 3D x-ray CT approaches can be used to estimate the quantity of residual tin. The x-ray CT results demonstrated a strong linear correlation ($r^2 = 0.92$) between volume of tin and total projected surface area of tin. Hence, 2D x-rays directly measuring projected area were also explored. The 2D approach detected similar patterns of tin as the 3D scans, but somewhat underestimated the total projected surface area of tin. This is likely due to resolution limitations with the film-based x-ray used in the experiments, but there is scope to improve this. It appears that the 2D approach is ideal for fast quality control checks on mass produced parts, while 3D x-ray CT is preferable for more accurate characterisation and research. The results indicate significant scope for reduction in residual tin quantities with improvement and refinement of the process: residual tin volume dropped from about 5.7 % in the early samples to about 1.6 % in the later samples.

Mechanical properties were assessed via interlaminar shear testing in three-point bending on small rectangular samples cut from the formed sheets and having known tin content (i.e. measured from the x-ray analysis). Results were compared to those from testing of samples produced without interlaminar tin sheets ('No Tin-P' and 'No Tin-R'). With refinement of the process, interlaminar shear strengths of 62.9 MPa were achieved and this is comparable to the 63.4 MPa achieved with control specimens produced without interlaminar tin ('No Tin-R'). There was, however, a reduction of about 26 % in the value of interlaminar shear stress at yield when the optimised tin based samples were compared with the radiant heated control samples. Furthermore, a number of tests exhibited a more ductile failure in the samples containing tin. A statistically significant, but weak, negative correlation was found between tin content and ILSS ($r^2 = 0.13$), ILL_{S_y} ($r^2 = 0.09$) when looking at the entire sample set. However, the significance of the finding disappeared when looking within individual samples. There is also evidence of results clustering based on manufactured sample. Given there were challenges in controlling the heating process and continuing variability between manufactured samples, this suggests that processing parameters such as temperature, pressure and cooling may influence both tin removal and mechanical properties. Other aspects such as the spatial distribution of the residual tin may be more significant (at least in our results) than tin quantity alone.

In summary, preliminary work on this new processing approach has already shown that parts with as little as 1.6 % residual tin can be formed and that interlaminar shear strength can be maintained at this level of tin content. Additional reductions in residual tin content are probable with further refinements and automation of the process (such as more controlled & uniform heating of the tin during forming). Finally, 2D x-rays are ideal for fast quality checks and 3D x-ray CT approaches are preferable for more accurate characterisation of residual tin content.

Table 6

Adjusted P-Values from linear regression on relationship between surface area of tin and selected mechanical properties. Significant results (<0.05) are shown in bold. A significant relationship appears when looking across all samples, but when data is segregated by sample this correlation disappears (Excluding ILL_{S_y} in Tin-IA2).

	ILSS (MPa)	ILL_{S_y} (MPa)
All Samples	0.01	0.02
Tin-IA1	0.27	0.18
Tin-IA2	0.54	0.03
Tin-IA3	0.32	0.89
Tin-IB4	0.96	0.80
Tin-IB5	0.21	0.34

CRediT authorship contribution statement

Iain Campbell: Conceptualization, Investigation, Visualization, Formal analysis, Writing – original draft. **Daniel M. Mulvihill:** Conceptualization, Writing – review & editing, Supervision. **Philip Harrison:** Conceptualization, Writing – review & editing, Supervision.

Declaration of Competing Interest

The authors declare that they have no known competing financial interests or personal relationships that could have appeared to influence the work reported in this paper.

Data availability

Data will be made available on request.

Acknowledgements

The authors would like to acknowledge the support of the Engineering and Physical Sciences Research Council (EPSRC) via a feasibility study funded by EP/P006701/1 and a DTA PhD studentship (for IC) funded by EP/N509668/1.

References

- European Commission. Setting CO2 emission performance standards for new passenger cars and for new light commercial vehicles, and repealing Regulations 2019.
- Krämer ETM. The formation of fiber waviness during thermoplastic composite laminate consolidation 2021. 10.3990/1.9789036552738.
- O'Brádaigh CM, Pipes RB, Mallon PJ. Issues in diaphragm forming of continuous fiber reinforced thermoplastic composites. *Polym Compos* 1991;12:246–56. <https://doi.org/10.1002/pc.750120406>.
- Harrison P, Gomes R, Curado-Correia N. Press forming a 0/90 cross-ply advanced thermoplastic composite using the double-dome benchmark geometry. *Compos Part A Appl Sci Manuf* 2013;54:56–69. <https://doi.org/10.1016/j.compositesa.2013.06.014>.
- Ahn H, Kuuttila NE, Pourboghrat F. Mechanical analysis of thermo-hydroforming of a fiber-reinforced thermoplastic composite helmet using preferred fiber orientation model. *J Compos Mater* 2018;52:3183–98. <https://doi.org/10.1177/0021998318762547>.
- Poppe C, Joppich T, Dörr D, Kärger L, Henning F. Modeling and validation of gripper induced membrane forces in finite element forming simulation of continuously reinforced composites. *AIP Conf Proc* 2017;1896:1–7. <https://doi.org/10.1063/1.5007989>.
- Liu K, Zhang B, Xu X, Ye J. Experimental characterization and analysis of fiber orientations in hemispherical thermostamping for unidirectional thermoplastic composites. *Int J Mater Form* 2019;12. <https://doi.org/10.1007/s12289-018-1410-y>.
- MacHado M, Murenu L, Fischlschweiger M, Major Z. Analysis of the thermomechanical shear behaviour of woven-reinforced thermoplastic-matrix composites during forming. *Compos Part A Appl Sci Manuf* 2016;86:39–48. <https://doi.org/10.1016/j.compositesa.2016.03.032>.
- Guzman-Maldonado E, Hamila N, Naour N, Moulin G, Boisse P. Simulation of the thermoplastic prepreg thermoforming based on a visco-hyperelastic model and a thermal homogenization. *Mater Des* 2016;93:431–42. <https://doi.org/10.1016/j.matdes.2015.12.166>.
- Thompson AJ, Belnoue JPH, Hallett SR. Modelling defect formation in textiles during the double diaphragm forming process. *Compos Part B Eng* 2020;202. <https://doi.org/10.1016/j.compositesb.2020.108357>.
- Potter K, Khan B, Wisnom M, Bell T, Stevens J. Variability, fibre waviness and misalignment in the determination of the properties of composite materials and structures. *Compos Part A Appl Sci Manuf* 2008. <https://doi.org/10.1016/j.compositesa.2008.04.016>.
- Vanclooster K. Forming of Multilayered Fabric Reinforced thermoplastic Composites. 2009.
- Harrison P, Campbell I, Guliyev E, McLelland B, Gomes R, Curado-Correia N, et al. Induction melt thermoforming of advanced multi-axial thermoplastic composite laminates. *J Manuf Process* 2020;60:673–83. <https://doi.org/10.1016/j.jmapro.2020.10.026>.
- Vella JR, Chen M, Stillinger FH, Carter EA, Debenedetti PG, Panagiotopoulos AZ. Structural and dynamic properties of liquid tin from a new modified embedded-atom method force field. *Phys Rev B* 2017;95:1–37. <https://doi.org/10.1103/PhysRevB.95.064202>.
- Gholizadeh S. A review of non-destructive testing methods of composite materials. *Procedia Struct. Integr.*, vol. 1, Elsevier B.V.; 2016, p. 50–7. 10.1016/j.prostr.2016.02.008.
- Wildenschild D, Sheppard AP. X-ray imaging and analysis techniques for quantifying pore-scale structure and processes in subsurface porous medium systems. *Adv Water Resour* 2013;51:217–46. <https://doi.org/10.1016/j.advwatres.2012.07.018>.
- Hsieh J. Computed Tomography: Principles, Design, Artifacts, and Recent Advances. SPIE 2015. <https://doi.org/10.1117/3.2197756>.
- Hubbel, J.H.I SMS. X-Ray Mass Attenuation Coefficients. NIST Stand Ref Database 126 n.d. <https://dx.doi.org/10.18434/74D01F>.
- More C V., Bhosale RR, Pawar PP. Detection of new polymer materials as gamma-ray-shielding materials. *Radiat Eff Defects Solids* 2017;172:469–84. 10.1080/10420150.2017.1336765.
- Yaffe MJ, Rowlands JA. X-ray detectors for digital radiography. *Phys Med Biol* 1997;42:1–39. <https://doi.org/10.1088/0031-9155/42/1/001>.
- Kane SN, Mishra A, Dutta AK. Preface: International Conference on Recent Trends in Physics (ICRTP 2016). *J Phys Conf Ser* 2016;755. 10.1088/1742-6596/755/1/011001.
- Jandjsek I, Jakubek J, Jakubek M, Prucha P, Krejci F, Soukup P, et al. X-ray inspection of composite materials for aircraft structures using detectors of Medipix type. *J Instrum* 2014;9. <https://doi.org/10.1088/1748-0221/9/05/C05062>.
- Cnudde V, Boone MN. High-resolution X-ray computed tomography in geosciences: A review of the current technology and applications. *Earth-Science Rev* 2013;123:1–17. <https://doi.org/10.1016/j.earscirev.2013.04.003>.
- Garcea SC, Wang Y, Withers PJ. X-ray computed tomography of polymer composites. *Compos Sci Technol* 2018;156:305–19. <https://doi.org/10.1016/j.compscitech.2017.10.023>.
- Tsao CC, Hocheng H. Computerized tomography and C-Scan for measuring delamination in the drilling of composite materials using various drills. *Int J Mach Tools Manuf* 2005;45:1282–7. <https://doi.org/10.1016/j.ijmactools.2005.01.009>.
- Nikishkov Y, Airoldi L, Makeev A. Measurement of voids in composites by X-ray Computed Tomography. *Compos Sci Technol* 2013;89:89–97. <https://doi.org/10.1016/j.compscitech.2013.09.019>.
- Hassen AA, Taheri H, Vaidya UK. Non-destructive investigation of thermoplastic reinforced composites. *Compos Part B Eng* 2016;97:244–54. <https://doi.org/10.1016/j.compositesb.2016.05.006>.
- Yu B, Bradley RS, Soutis C, Withers PJ. A comparison of different approaches for imaging cracks in composites by X-ray microtomography. *Philos. Trans. R. Soc. A Math. Phys. Eng. Sci.*, vol. 374, Royal Society of London; 2016. 10.1098/rsta.2016.0037.
- Marshall SJ, Bayne SC, Baier R, Tomsia AP, Marshall GW. A review of adhesion science. *Dent Mater* 2010;26:e11–6. <https://doi.org/10.1016/j.dental.2009.11.157>.
- García D, Starkweather HW. Hydrogen bonding in nylon 66 and model compounds 1984;23. 10.1002/pol.1985.180230310.
- INTERNATIONAL STANDARD. EN ISO 14130 : Fiber-reinforced plastic composites Determination of interlaminar shear strength. *Int Stand* 1997.
- Chowdhury IR, Nash NH, Portela A, O'Dowd NP, Comer AJ. Analysis of failure modes for a non-crimp basalt fiber reinforced epoxy composite under flexural and interlaminar shear loading. *Compos Struct* 2020;245. <https://doi.org/10.1016/j.compstruct.2020.112317>.
- He Y, Makeev A. Nonlinear shear behavior and interlaminar shear strength of unidirectional polymer matrix composites: A numerical study. *Int J Solids Struct* 2014. <https://doi.org/10.1016/j.ijsolstr.2013.12.014>.
- Cho D, Yun SH, Kim J, Lim S, Park M, Lee G, et al. Effects of Fiber Surface-Treatment and Sizing on the Dynamic Mechanical and Interfacial Properties of Carbon / Nylon 6. *Composites* 2004;5:1–5.
- Yao L, Lu Y, Li Z, Li S, Wu B, Yang C. Effect of surface post-oxidation of epoxy-sized carbon fibre on interlaminar shear strength of the polyamide 66 composites. *Compos Interfaces* 2020. <https://doi.org/10.1080/09276440.2020.1802166>.
- Yi JW, Lee W, Seong DG, Won HJ, Kim SW, Um MK, et al. Effect of phenoxo-based coating resin for reinforcing pitch carbon fibers on the interlaminar shear strength of PA6 composites. *Compos Part A Appl Sci Manuf* 2016;87:212–9. <https://doi.org/10.1016/j.compositesa.2016.04.028>.
- Caminero MA, Chacón JM, García-Moreno I, Reverte JM. Interlaminar bonding performance of 3D printed continuous fibre reinforced thermoplastic composites using fused deposition modelling. *Polym Test* 2018;68:415–23. <https://doi.org/10.1016/j.polymertesting.2018.04.038>.
- Yavas D, Zhang Z, Liu Q, Wu D. Interlaminar shear behavior of continuous and short carbon fiber reinforced polymer composites fabricated by additive manufacturing. *Compos Part B Eng* 2021;204:108460. <https://doi.org/10.1016/j.compositesb.2020.108460>.
- Bienias J, Jakubczak P, Drożdździł M, Surowska B. Interlaminar shear strength and failure analysis of aluminium-carbon laminates with a glass fiber interlayer after moisture absorption. *Materials (Basel)* 2020;13:1–14. <https://doi.org/10.3390/ma13132999>.
- Jakubczak P, Bienias J, Surowska B. Interlaminar shear strength of fibre metal laminates after thermal cycles. *Compos Struct* 2018;206:876–87. <https://doi.org/10.1016/j.compstruct.2018.09.001>.
- Bellini C, Di Cocco V, Sorrentino L. Interlaminar shear strength study on CFRP/Al hybrid laminates with different properties. *Frat Ed Integrita Strutt* 2020;14:442–8. <https://doi.org/10.3221/IGF-ESIS.51.32>.
- Bellini C, Di Cocco V, Iacoviello F, Sorrentino L. Influence of structural characteristics on the interlaminar shear strength of CFRP/Al fibre metal laminates. *Procedia Struct. Integr.*, vol. 18, Elsevier B.V.; 2019, p. 373–8. 10.1016/j.prostr.2019.08.177.

- [43] Dong F, Meschter SJ, Cho J. Improved adhesion of polyurethane-based coatings to tin surface. *J Mater Sci Mater Electron* 2019;30:7268–79. <https://doi.org/10.1007/s10854-019-01040-6>.
- [44] Tencate. Tencate Cetex TC1200. Co Website 2014:95037. https://www.toraytac.com/media/694245aa-3765-43b4-a2cd-8cf76e4aec5/lmhlVg/TAC/Documents/Data_sheets/Thermoplastic/UD tapes, prepregs and laminates/Toray-Cetex-TC910_PA6_PDS.pdf (accessed November 22, 2021).
- [45] Silicones S. *Silicone Rubber Sheeting High Temperature Solid - Data Sheet*. Silix Silicones Ltd 2019.
- [46] Lona Batista N, Anagnostopoulos K, Cocchieri Botelho E, Kim H. Influence of crystallinity on interlaminar fracture toughness and impact properties of polyphenylene sulfide/carbon fiber laminates. *Eng Fail Anal* 2021;119:104976. <https://doi.org/10.1016/j.engfailanal.2020.104976>.
- [47] Chen H, Li S, Wang J, Ding A. A focused review on the thermo-stamping process and simulation progresses of continuous fibre reinforced thermoplastic composites. *Compos Part B Eng* 2021;224:109196. <https://doi.org/10.1016/j.compositesb.2021.109196>.
- [48] Taketa I, Kalinka G, Gorbatiikh L, Lomov SV, Verpoest I. Influence of cooling rate on the properties of carbon fiber unidirectional composites with polypropylene, polyamide 6, and polyphenylene sulfide matrices. *Adv Compos Mater* 2020;29:101–13. <https://doi.org/10.1080/09243046.2019.1651083>.
- [49] Barrett JF, Keat N. Artifacts in CT : Recognition and Avoidance. *Radiographics* 2004;24:1679–91. <https://doi.org/10.1148/rg.246045065>.
- [50] Kapur JN, Sahoo PK, Wong AKC. A new method for gray-level picture thresholding using the entropy of the histogram. *Comput Vision, Graph Image Process* 1985;29:273–85. [https://doi.org/10.1016/0734-189X\(85\)90125-2](https://doi.org/10.1016/0734-189X(85)90125-2).
- [51] Makeev A, He Y, Schreier H. Short-beam shear method for assessment of stress-strain curves for fibre-reinforced polymer matrix composite materials. *Strain* 2013;49:440–50. <https://doi.org/10.1111/str.12050>.
- [52] Palazzetti R, Zucchelli A. Electrospun nanofibers as reinforcement for composite laminates materials – A review. *Compos Struct* 2017;182:711–27. <https://doi.org/10.1016/j.compstruct.2017.09.021>.
- [53] Ou Y, González C, Vilatela JJ. Understanding interlaminar toughening of unidirectional CFRP laminates with carbon nanotube veils. *Compos Part B Eng* 2020;201. <https://doi.org/10.1016/j.compositesb.2020.108372>.
- [54] Beylergil B, Tanoğlu M, Aktaş E. Effect of polyamide-6,6 (PA 66) nonwoven veils on the mechanical performance of carbon fiber/epoxy composites. *Compos Struct* 2018;194:21–35. <https://doi.org/10.1016/j.compstruct.2018.03.097>.
- [55] Brugo T, Minak G, Zucchelli A, Yan XT, Belcari J, Saghafi H, et al. Study on Mode I fatigue behaviour of Nylon 6,6 nanoreinforced CFRP laminates. *Compos Struct* 2017;164:51–7. <https://doi.org/10.1016/J.COMPSTRUCT.2016.12.070>.
- [56] Ou Y, González C, Vilatela JJ. Interlaminar toughening in structural carbon fiber/epoxy composites interleaved with carbon nanotube veils. *Compos Part A Appl Sci Manuf* 2019;124:105477. <https://doi.org/10.1016/j.compositesa.2019.105477>.
- [57] Shuler SF, Advani SG. Transverse squeeze flow of concentrated aligned fibers in viscous fluids. *J Nonnewton Fluid Mech* 1996;65:47–74. [https://doi.org/10.1016/0377-0257\(96\)01440-1](https://doi.org/10.1016/0377-0257(96)01440-1).